AJNR Am J Neuroradiol 23:67–75, January 2002

High-Resolution Line Scan Diffusion Tensor MR Imaging of White Matter Fiber Tract Anatomy

Hatsuho Mamata, Yoshiaki Mamata, Carl-Fredrik Westin, Martha E. Shenton, Ron Kikinis, Ferenc A. Jolesz, and Stephan E. Maier

BACKGROUND AND PURPOSE: **MR diffusion tensor imaging permits detailed visualization of white matter fiber tracts. This technique, unlike T2-weighted imaging, also provides information about fiber direction. We present findings of normal white matter fiber tract anatomy at high resolution obtained by using line scan diffusion tensor imaging.**

METHODS: **Diffusion tensor images in axial, coronal, and sagittal sections covering the entire brain volume were obtained with line scan diffusion imaging in six healthy volunteers. Images were acquired for b factors 5 and 1000 s/mm^2 at an imaging resolution of 1.7 × 1.7 × 4 mm. For selected regions, images were obtained at a reduced field of view with a spatial resolution of 0.9 × 0.9 × 3 mm. For each pixel, the direction of maximum diffusivity was computed and used to display the course of white matter fibers.**

RESULTS: **Fiber directions derived from diffusion tensor imaging were consistent with known white matter fiber anatomy. The principal fiber tracts were well observed in all cases. The tracts that were visualized included the following: the arcuate fasciculus; superior and inferior longitudinal fasciculus; uncinate fasciculus; cingulum; external and extreme capsule; internal capsule; corona radiata; auditory and optic radiation; anterior commissure; corpus callosum; pyramidal tract; gracile and cuneatus fasciculus; medial longitudinal fasciculus; rubrospinal, tectospinal, central tegmental, and dorsal trigeminothalamic tract; superior, inferior, and middle cerebellar peduncle; pallidonigral and strionigral fibers; and root fibers of the oculomotor and trigeminal nerve.**

CONCLUSION: **We obtained a complete set of detailed white matter fiber anatomy maps of the normal brain by means of line scan diffusion tensor imaging at high resolution. Near large bone structures, line scan produces images with minimal susceptibility artifacts.**

Before the advent of advanced MR imaging techniques, the investigation of white matter anatomy had been limited to the evaluation of gross brain sections with myelin-specific stains or to the dissection of fibers of formalin-fixed brains. Conventional T2-weighted MR imaging offers excellent contrast between white and gray matter, without, however, providing any information about fiber direction. A rat brain atlas has been acquired with 2D thin-section MR imaging (1) and a mouse lemur atlas with 3D microscopic MR imaging (2). Fluid-attenuated inversion recovery T2-weighted imaging has been introduced to attain improved visualization of the white matter tracts within the brain stem (3). Magnetization transfer MR imaging is another technique that has been applied to white matter imaging (4–6); however, with any of the MR techniques mentioned above, the direction of the fibers in white matter tracts cannot be shown, and therefore, they cannot provide complete anatomic information about white matter fiber tracts.

MR diffusion imaging reveals the diffusion of water molecules. The direction of highest diffusivity coincides with the white matter tissue's fiber tract axis (7, 8). Variation of the diffusion along different spatial directions provides information about diffusion an-

Received April 17, 2001; accepted after revision August 15.

From the Department of Radiology, Brigham and Women's Hospital (H.M., Y.M., C.-F.W., M.E.S., R.K., F.A.J., S.E.M.), the Clinical Neuroscience Division (M.E.S.), Laboratory of Neuroscience, VAMC-Brockton, Department of Psychiatry, Harvard Medical School, Boston, MA; and the Department of Radiology (H.M.), Tokai University School of Medicine, Bohseidai, Isehara, Kanagawa, Japan.

Supported by the Whitaker Foundation, the National Institutes of Health (NIH 1 R01 NS39335–01A1, NIH 5 P41 RR13218–01, NIMH R01 50747, and NIMH K02 01110), and the Veterans Administration Merit Award.

Presented at the Radiological Society of North America Meeting, 2000, and presented in part at the 8th Scientific Meeting and Exhibition of the International Society for Magnetic Resonance in Medicine, 2000, Denver, CO.

Address reprint requests to Hatsuho Mamata, Department of Radiology, Brigham and Women's Hospital, 75 Francis Street, Boston, MA 02115.

© American Society of Neuroradiology

isotropy and ultimately about tissue structure (9, 10). The principal diffusion direction and diffusion anisotropy can be assessed with diffusion tensor imaging.

The purpose of the present study was to obtain detailed white matter fiber tract anatomy of the whole brain with a diffusion tensor imaging technique that yields minimal distortion artifacts near large bone structures and air cavities as well as unprecedented high spatial resolution. To attain this goal, we used line scan diffusion imaging (11) in conjunction with high-performance magnetic field gradients.

Methods

Participants and Imaging Protocol

Six healthy volunteers (four men and two women; age range, 35–45 years) were entered into the study. No participant had a neurologic disorder or any abnormality revealed by T1- or T2-weighted imaging of the brain. All studies were conducted within the guidelines of the research committee at our institution. Written informed consent was obtained from all participants.

The protocol included T1-weighted imaging for localization and line scan diffusion tensor imaging of the entire brain in axial, sagittal, and/or coronal sections. Thin-section, high-resolution line scan diffusion tensor images of the brain stem were also obtained in axial, sagittal, and/or coronal orientations. Line scan diffusion imaging uses multiple diffusion-weighted spin-echo column excitations to form a 2D image. The basic sequence is composed of a selective $\pi/2$ pulse and a selective π pulse with diffusion gradients on both sides of the refocusing π pulse, followed by a standard frequency-encoding readout along the selected column. The sequential collection of these line data in independent acquisitions makes the sequence largely insensitive to bulk motion artifacts. Spatial interleaving of the column excitation allows for uniform sampling with overlapping column cross sections and minimal T1 weighting. Multiple sections can be obtained in sequential images and the imaging time, therefore, is proportional to the number of sections acquired. Because no phase encoding is applied, chemical shift and susceptibility artifacts are present only in the frequency-encoding direction and, like chemical shift and susceptibility artifacts in conventional spin-echo imaging, are determined by the applied bandwidth.

All studies were performed on a 1.5-T whole-body MR system (LX Echospeed Cvi; General Electric Medical System, Milwaukee, WI) with version 8.2.5 software. The imager is equipped with magnetic field gradients that permit up to 40 mT/m amplitude. A quadrature birdcage head coil was used for all images, with the exception of images obtained with a surface coil to show subcortical U-fibers.

T1-weighted imaging for localization was performed with a standard spin-echo sequence: 750/14/1 (TR/TE/NEX); field of view, 220 mm; section thickness, 5 mm; section gap, 1 mm; matrix size, 256 × 256; bandwidth, ±15.6 kHz. Axial and coronal sections for diffusion tensor imaging were planned orthogonal to a midline sagittal T1-weighted image. The axial sections were slightly oblique, parallel to the anterior-posterior commissure line, and the coronal sections were angulated, perpendicular to the anterior-posterior commissure line. The orientation of sagittal sections was planned on axial localizing images. Depending on participant and section orientation, 24 to 34 sections were sufficient to cover the entire brain.

Line scan diffusion images were obtained with the following parameters: 2560/80/66/1 (effective TR relevant for T1 weighting [11]/TR/TE/NEX); rectangular field of view, 220 × 165 mm; effective section thickness, 4 mm [11]; section gap, 1 mm; matrix size, 128 × 96 (frequency × column); bandwidth, ±3.91 kHz. To measure the apparent diffusion coefficient, images were scanned at two different diffusion weightings (b factors, 5 and 1000 s/mm^2; gradient pulse duration δ, 21.2 ms; separation Δ between first and second gradient pulse, 33 ms; gradient amplitude, 40 mT/m (ie, two gradient main directions applied simultaneously at 70% of the maximal attainable amplitude). Diffusion weighting for the high b factor was applied along six non-collinear directions (8, 9) (relative amplitudes, $[G_x,G_y,G_z]$ = [1,1,0], [0,1,1], [1,0,1], [0,1,−1], [1,−1,0], [−1,0,1]), whereas for the low b factor, diffusion weighting was applied along two directions only. Collection of image data for all gradient configurations at low diffusion weighting is not necessary, because the directionally dependent, diffusion-related signal attenuation is minimal. A minimal diffusion encoding of 5 s/mm^2 is required, because with the present sequence implementation, the diffusion-encoding gradients also act as spin-echo crusher gradients. Two diffusion-weighted images instead of only one are acquired for various reasons, such as reduction of average gradient load and optimal cancellation of secondary echoes. The imaging time was 61 s per section (ie, the time required for complete coverage of the brain along one orientation was between 25 and 35 min). Shorter TEs, TRs, and imaging times would have been possible had gradient heating not been a concern. Images of the brain stem and subcortical U-fibers were obtained with the same diffusion gradient configuration at a reduced section thickness of 3 mm and a section gap of 0 mm. Other imaging parameters were as follows: 2178/99/76; rectangular field of view, 220 × 55 mm; matrix size, 256 × 64 (frequency × column); bandwidth, ±3.91 kHz. For optimal signal-to-noise ratio, four averages were acquired for head coil scans and one average only for surface coil scans.

Postprocessing

The term "tensor" originates from the physics and engineering field, where it was introduced to describe tension forces in solid bodies with an array of 3D vectors. The particular tensors used to describe diffusion can be further conceptualized and visualized as ellipsoids. The longest of the three orthogonal main axes of the diffusion ellipsoid represents the value (eigenvalue) and direction (eigenvector) of maximum diffusion, whereas the shortest axis denotes the value and direction of minimum diffusion. If the length of the three axes is equal, then the diffusion is said to be isotropic and the diffusion tensor can be visualized as a sphere. For example, in the case of CSF or gray matter, the diffusion tensor is best characterized by spherical, or isotropic, diffusion. If the length of the three axes differs, the diffusion is said to be anisotropic. The diffusion tensor data were processed off-line. For each section, a T2-weighted map (average of the two images obtained at low diffusion weighting), a trace diffusion-weighted map, a trace apparent diffusion coefficient map, and a relative anisotropy map were calculated. In addition, maps of the principal effective diffusivities (eigenvalues $\lambda 1$, $\lambda 2$, and $\lambda 3$) as well as the eigenvector components x, y, and z of the largest eigenvalue $\lambda 1$ were computed. Dedicated software was used to visualize fiber directions with the eigenvector of the largest eigenvalue superposed on an anatomic background image (12). To highlight gray and white matter areas, T2-weighted images were used as background maps. The eigenvector of the largest eigenvalue (first eigenvector) is thought to represent the fiber direction (7, 13). For each pixel, a line representing the in-plane component of the measured fiber direction is drawn. The length of the line is proportional to the relative anisotropy. Dots on color images represent pixels where the through-plane component (vertical to the plane) of the scaled first eigenvector reaches a predefined threshold. Masks, based on signal thresholds in images with high diffusion weighting, were used to limit the representation of the eigenvectors to areas with brain tissue.

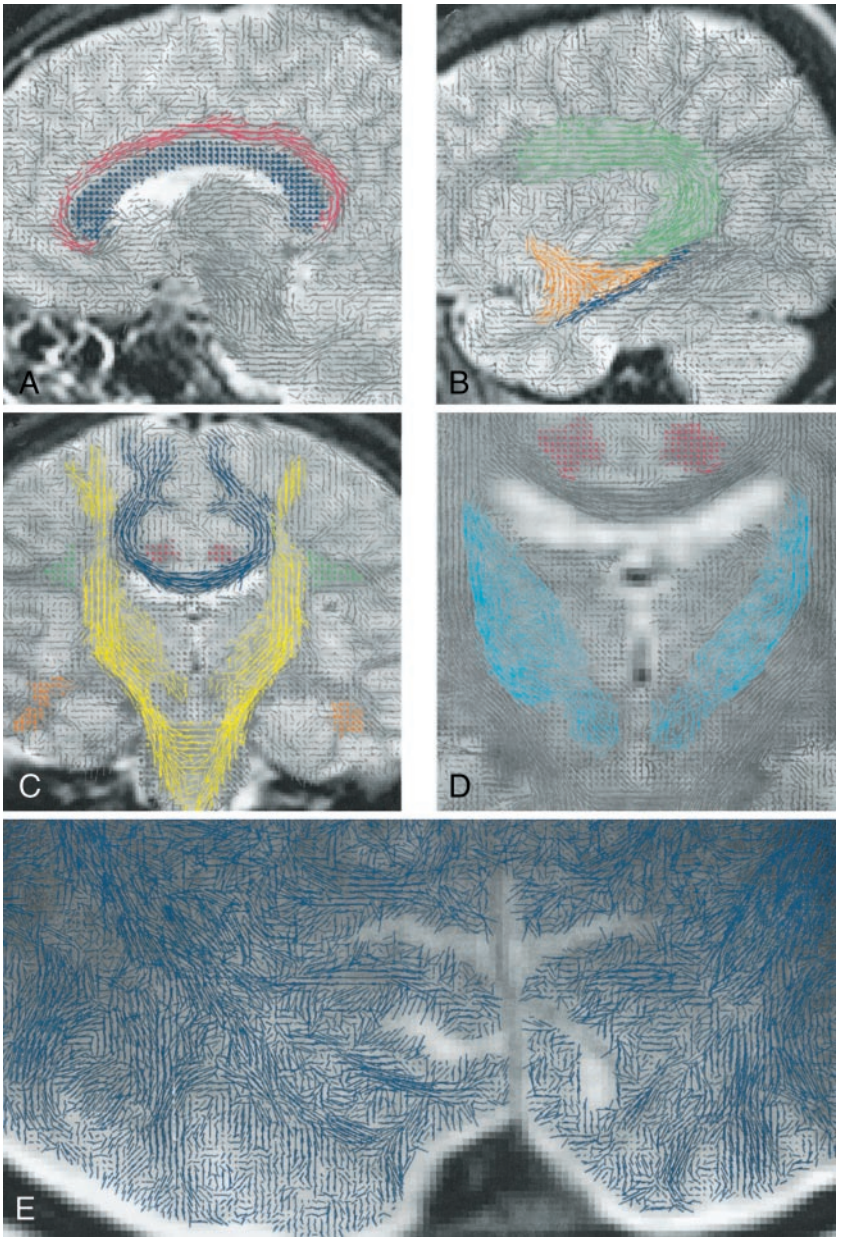

FIG 1. When viewed in multiple sections, the appearance of the association fibers on the principal eigenvector maps is consistent with known anatomy.

A, Sagittal 110 × 110-mm subimage close to the midline, passing through the cingulum (*pink*). Note that the fibers of the corpus callosum run at a slight angle through the plane (*blue dots with short lines*).

B, More lateral sagittal section obtained through the arcuate fasciculus (*green*), inferior longitudinal fasciculus (*blue*), and uncinate fasciculus (*orange*).

C, Coronal section obtained at the level of the posterior limb of the internal capsule. Fibers of the cingulum (*pink*), arcuate fasciculus (*green*), and uncinate fasciculus (*orange*) pass through the section (*dots*). Fibers of the posterior limb of the internal capsule (*yellow lines*) are running in-plane.

D, High-resolution 55 × 55-mm coronal subimage of the thalamic region. The strionigral and pallidonigral fibers are shown in *light blue*.

E, High-resolution axial surface coil image of the calcarine area at a 120 × 60-mm field of view. U-fibers connecting visual cortices are well seen.

For some images, masks were defined manually to exclude areas with fatty tissue in the skull and skin.

Characterization of White Matter Fiber Anatomy

The eigenvector maps were compared with histologic cross sections found in anatomy books (14, 15). The search for white matter tracts on these eigenvector maps was focused on *association fibers* (cingulum, arcuate fasciculus, superior and inferior longitudinal fasciculus, uncinate fasciculus, pallidonigral and strionigral fibers, U-fibers), *projection fibers* (corona radiata, internal capsule, auditory and optic radiation), and *commissural fibers* (corpus callosum and anterior commissure). The following structures were also studied: root fibers of the oculomotor nerve; optic tract; pyramidal (corticospinal) tract in the cerebral peduncle; decussation of the superior cerebellar peduncle; rubrospinal tract; medial longitudinal fasciculus; tectospinal tract; central tegmental tract; dorsal trigeminothalamic tract; spinothalamic tract; pyramidal tract in the pons and frontopontine tract; superior, inferior, and middle cerebellar peduncle; root fibers of trigeminal nerve; pyramidal decussation; sensory decussation; and pontocerebellar fibers.

Results

The description of the findings follows the traditional anatomic separation into association fibers, projection fibers, commissural fibers, and fibers of brain stem and cerebellum. The images originate from different participants; however, the tracts described were observed in all cases.

Association Fibers

The best gross view of the association fibers is shown on sagittal images (Figs 1 and 2). The course of these fibers, however, cannot be followed in a single section. When viewed in multiple sections, the ap-

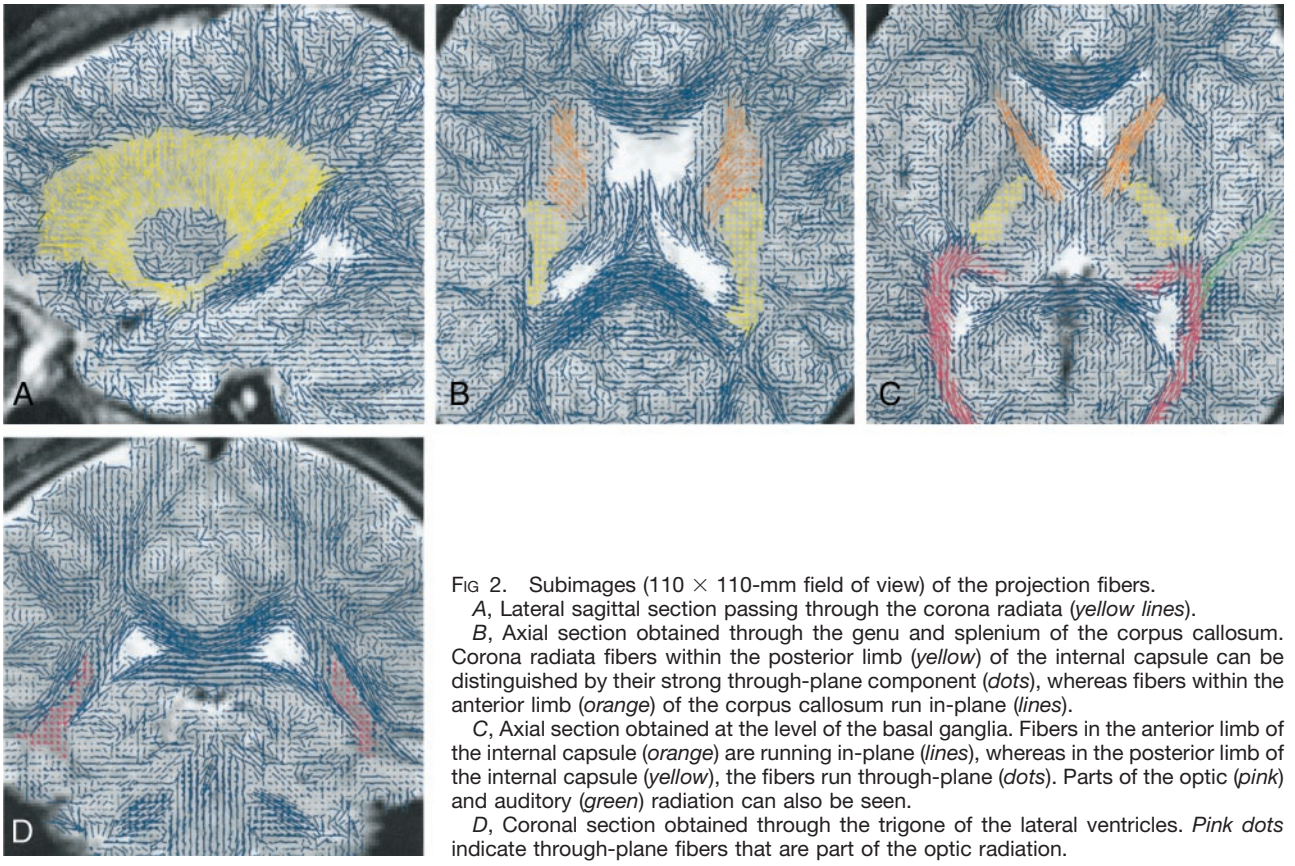

FIG 2. Subimages (110 × 110-mm field of view) of the projection fibers.
A, Lateral sagittal section passing through the corona radiata (*yellow lines*).
B, Axial section obtained through the genu and splenium of the corpus callosum. Corona radiata fibers within the posterior limb (*yellow*) of the internal capsule can be distinguished by their strong through-plane component (*dots*), whereas fibers within the anterior limb (*orange*) of the corpus callosum run in-plane (*lines*).
C, Axial section obtained at the level of the basal ganglia. Fibers in the anterior limb of the internal capsule (*orange*) are running in-plane (*lines*), whereas in the posterior limb of the internal capsule (*yellow*), the fibers run through-plane (*dots*). Parts of the optic (*pink*) and auditory (*green*) radiation can also be seen.
D, Coronal section obtained through the trigone of the lateral ventricles. *Pink dots* indicate through-plane fibers that are part of the optic radiation.

pearance of the association fibers on the principal eigenvector maps is consistent with known anatomy. The main bundle of the cingulum is observed in a medial sagittal section (Fig 1A). The posterolateral branching bundle of the cingulum that connects with the parahippocampal area is observed on more lateral sections. The middle part of the arcuate fasciculus and almost the entire course of the superior longitudinal fasciculus are observed on a lateral section obtained through the insula (Fig 1B). The inferior longitudinal fasciculus connecting to the temporal lobe may be seen on the same section. Moreover, this particular section also shows the portion of the uncinate fasciculus that radiates into the temporal lobe. The main bundle of the uncinate fasciculus can be seen in a section more medial to the one shown in Fig 1B. In coronal images, all of these association fibers are shown running vertical to the plane (Fig 1C). The strionigral and pallidonigral fibers are observed in coronal image sections through the basal ganglia (Fig 1D). U-fibers connecting different cortical areas can be seen in multiple section locations. Figure 1E shows U-fibers in the occipital subcortex.

Projection Fibers

The fan-shaped appearance of the corona radiata, which connects the internal capsule with subcortical areas, is observed on multiple lateral sagittal views (Fig 2A). An axial view of the upper portion of the corona radiata is shown in Figure 2B. Figure 2C shows an axial view of the internal capsule at the level of the basal ganglia. On this axial image, the anterior limb of the internal capsule is shown as a bundle of dense in-plane fibers and in the posterior limb, the fibers run predominantly through the plane. A coronal view of the posterior limb of the internal capsule is shown in Figure 1C. On axial images, parts of the optic and auditory (Fig 2C) radiation can be seen. On a coronal image obtained through the posterior horn of the lateral ventricle (Fig 2D), the geniculocalcarine tract of the optic radiation is observed.

Commissural Fibers

The commissural fibers of the corpus callosum are observed in sections obtained near the lateral ventricle. In the particular section shown in Figure 2C, the genu of the corpus callosum contains mainly the fibers that interconnect the medial parts of the frontal lobes. The body of the corpus callosum with fibers originating from the posterior part of the frontal lobe and the parietal lobe can be seen in Figures 1C and 3A. The splenium, shown on an axial image in Figure 2C and on a coronal image in Figure 2D, contains the fibers that interconnect corresponding areas of the temporal and occipital lobes. The fibers crossing within the anterior commissure are clearly shown in the coronal section in Figure 3B. On the adjacent coronal section (Fig 3A), the fibers of the anterior commissure can be seen radiating toward the temporal lobes. The frontal part of the anterior commissure

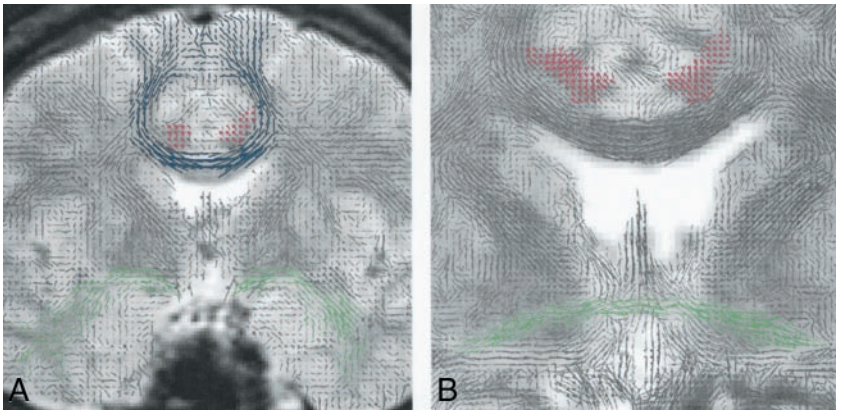

FIG 3. Commissural fibers of the corpus callosum are observed in sections obtained near the lateral ventricle.

A, Coronal section obtained through the insula (110 × 110-mm subimage). In this section, the cingulum (*pink*) and fibers (*blue*) interconnecting the frontoparietal cortices of each hemisphere with the corpus callosum can be seen. The fibers of the anterior commissure (*green*) radiate into the temporal lobes.

B, High resolution coronal section (55 × 55-mm subimage) obtained at the level of the anterior commissure (*green*).

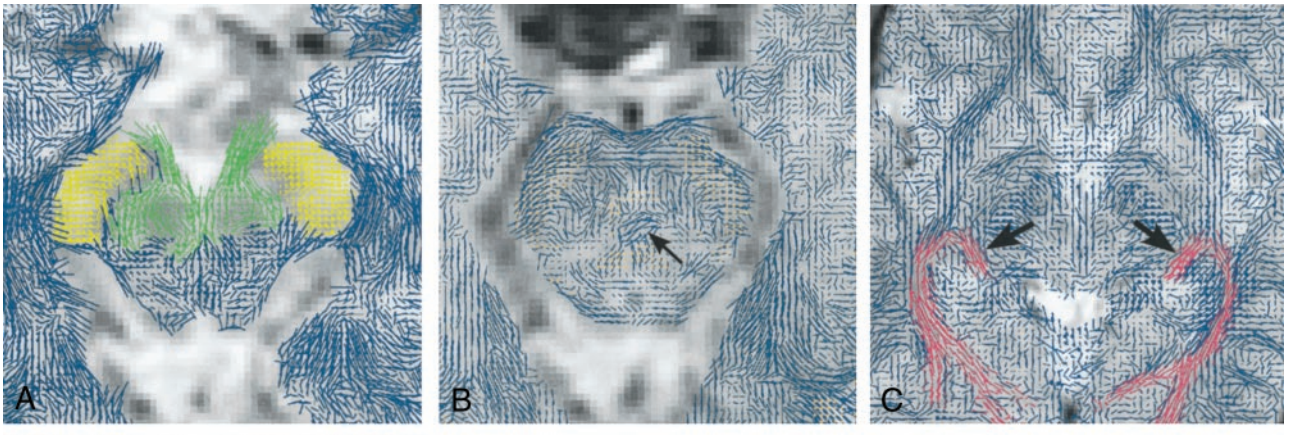

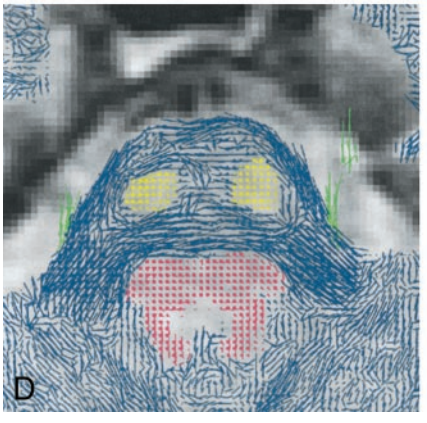

FIG 4. Subimages (55 × 55-mm field of view) of the brain stem.

A, Axial section obtained at the level of the upper midbrain. Very fine fibers that originate from the oculomotor nucleus run through and around the red nucleus and converge to the roots of the oculomotor nerves (*green*). Note that fibers of the cerebral peduncles are running at a slight angle through the plane (*yellow dots with lines*).

B, Axial section obtained at the level of the lower midbrain. The *arrow* indicates the decussation of the superior cerebellar peduncle.

C, Axial section (110 × 110-mm field of view) obtained at the level of the midbrain-cerebrum junction. The fibers of the optic tract (*arrows*) connect to the lateral geniculate bodies. Fibers of the optic radiation (*pink*) pass lateral to the optic tract.

D, Axial section obtained at the level of the pons, through the roots of the trigeminal nerve (*green*). Fibers of the craniocaudal tracts (superior cerebellar peduncle, medial longitudinal fasciculus, tectospinal tract, dorsal and ventral trigeminothalamic tracts, central tegmental tract, spinothalamic tract, and rubrospinal tract) can be seen in the posterior part of the pons (*pink*). The *yellow dots* indicate fibers of the pyramidal and the frontopontine tracts.

is known to be a very thin, small bundle of fibers interconnecting the olfactory bulbs. We failed to show this bundle of fibers in any sections obtained in this study.

Fibers of Brain Stem and Cerebellum

Small fiber bundles that pass through and around the red nucleus and converge to the rootlets of the oculomotor nerve can be observed on an axial image obtained through the midbrain (Fig 4A). The cerebral peduncles are easily separated from surrounding fiber tracts because of their craniocaudal direction component, which is represented as yellow and dark yellow dots on the axial plane maps (Fig 4A and B). In the section shown in Figure 4A, the optic tracts are shown coursing anterior to the cerebral peduncles. Their connection to the lateral geniculate bodies can be found in more cephalad sections (Fig 4C). In the center of a more caudal axial section of the midbrain, the decussation of the superior cerebellar peduncle is shown (Fig 4B). Ventral to the decussation of the superior cerebellar peduncle, the rubrospinal tract with fibers in a craniocaudal direction (dots) is observed. Dots dorsal to the decussation, as seen in Figure 4B, represent the craniocaudal fibers of the medial longitudinal fasciculus as well as the tectospinal, central tegmental, and dorsal trigeminothalamic tract. Visual separation of these tracts, however, based on either fiber direction or anisotropy, is not possible. At the level of the pons (axial section in Fig 4D), craniocaudal fibers belonging to the superior

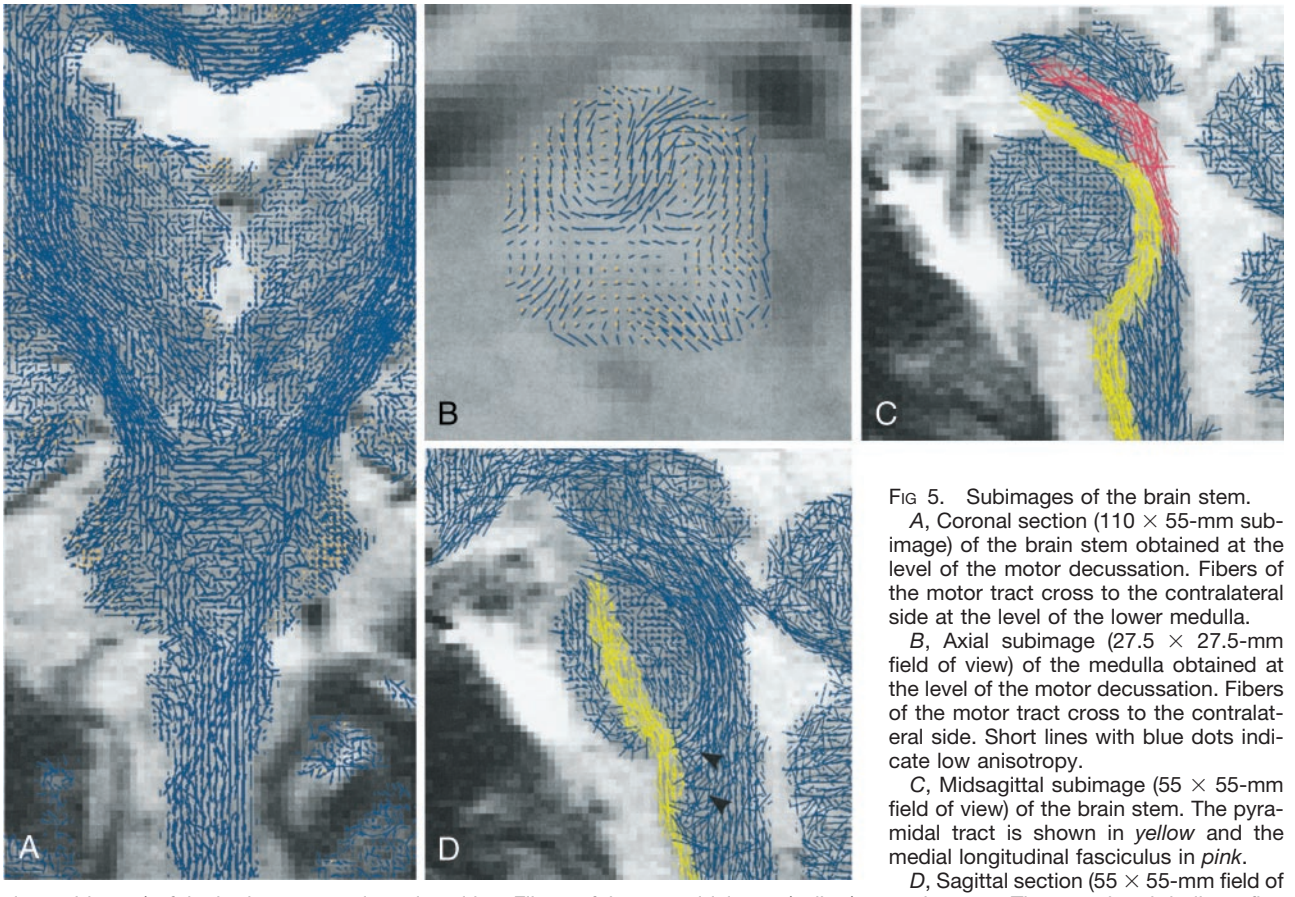

FIG 5. Subimages of the brain stem.
A, Coronal section (110 × 55-mm subimage) of the brain stem obtained at the level of the motor decussation. Fibers of the motor tract cross to the contralateral side at the level of the lower medulla.
B, Axial subimage (27.5 × 27.5-mm field of view) of the medulla obtained at the level of the motor decussation. Fibers of the motor tract cross to the contralateral side. Short lines with blue dots indicate low anisotropy.
C, Midsagittal subimage (55 × 55-mm field of view) of the brain stem. The pyramidal tract is shown in *yellow* and the medial longitudinal fasciculus in *pink*.
D, Sagittal section (55 × 55-mm field of view subimage) of the brain stem at a lateral position. Fibers of the pyramidal tract (*yellow*) enter the pons. The *arrowheads* indicate fine fibers of the sensory decussation (internal arcuate fibers), running in an anteroposterior direction.

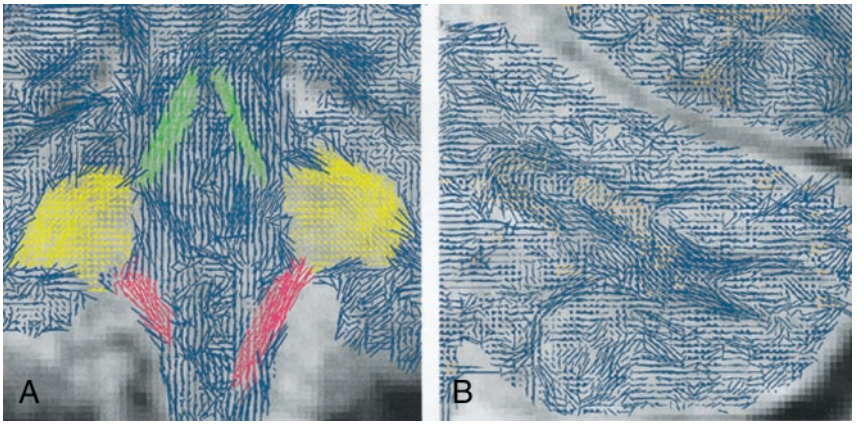

FIG 6. Subimages (55 × 55-mm field of view) of the cerebellum.
A, Coronal section obtained at the level of the fourth ventricle floor. Fibers of the superior (*green*) and inferior (*pink*) cerebellar peduncles pass in a craniocaudal direction toward the cerebellar hemisphere, and fibers of the middle cerebellar peduncle (*yellow*) pass at an oblique angle through the section (*dots with lines*).
B, More posterior coronal section of the cerebellum. Fibers from the cerebellar peduncles branch out toward the cerebellar cortices.

cerebellar peduncle, medial longitudinal fasciculus, tectospinal tract, dorsal and ventral trigeminothalamic tracts, central tegmental tract, spinothalamic tract, as well as the rubrospinal tract can be seen in the dorsal part, anterior to the fourth ventricle. Again, visual separation of the individual tracts with diffusion-weighted imaging seems not feasible. Along the cisternal side of the pons, fibers of the middle cerebellar peduncles traverse between each cerebellar hemisphere. Moreover, the axial section presented in Figure 4D shows the bilateral roots of the trigeminal nerve emerging from the pons into the prepontine cistern. Posterior to the middle cerebellar peduncle fibers, the frontopontine tract and the pyramidal tract can be seen coursing in a craniocaudal direction (Fig 4D).

On a coronal image obtained through the ventral medulla (Fig 5A), a long section of the pyramidal tract, from the posterior limb of the internal capsule via the cerebral peduncles down to the decussation within the lower medulla, can be seen concurrently. An axial view of the motor decussation is shown in Figure 5B. The corticospinal pathway of the pyramidal tract along the ventral portion of the medulla is

shown in a midsagittal section (Fig 5C) of the brain stem. Moreover, the corticobulbar pathway of the pyramidal tract can be seen passing along the posterior portion of the pons. On the same section following the base of the fourth ventricle toward midbrain, the medial longitudinal fasciculus can be observed. Furthermore, pontocerebellar fibers running orthogonal to the plane are readily distinguished. On a sagittal section obtained through the fornix (Fig 5D), the internal arcuate fibers of the sensory decussation can be seen coursing in anteroposterior direction.

On an axial image of the medulla, shown in Figure 5B, an area with low anisotropy (*short lines with blue dots*) is recognized dorsal to the motor decussation. This area corresponds to the central gray matter and the bilateral nucleus cuneatus.

On a coronal image obtained through the fourth ventricle floor in Figure 6A, fibers of the superior and inferior cerebellar peduncles can be seen passing along the fourth ventricle wall in craniocaudal direction. In the same section, the middle cerebellar peduncle runs in anteroposterior direction in this section. In a more posterior coronal section (Fig 6B), the fibers of the cerebellar peduncles can be seen branching out toward the cerebellar cortex.

Discussion

In the present study, line scan diffusion imaging was applied to collect diffusion tensor data of the human brain. Line scan diffusion imaging was used because it offers excellent image quality and spatial resolution. Moreover, line scan diffusion imaging is insensitive to bulk motion. Chemical shift and magnetic field susceptibility artifacts are minimal (11, 16, 17). Echo-planar imaging, which also is available at our institution, is equally sensitive to bulk motion but requires fat suppression and is limited by susceptibility-related image distortions in areas close to bone and air-filled structures (18, 19). With the massive skull base bone structure and air-filled spaces, susceptibility-related image distortions become a critical issue in imaging the brain stem. Line scan diffusion imaging is almost free of such artifacts and therefore is particularly suited to show detailed white matter fiber anatomy in these areas. Line scan diffusion imaging compared with echo-planar imaging requires longer imaging times. Nevertheless, complete brain coverage at high spatial resolution is feasible in approximately half an hour. Missregistration within this imaging time is not an issue: sections are acquired sequentially, each section in less time than with an interleaved multisection echo-planar imaging diffusion tensor image. Shorter imaging time and improved signal-to-noise ratio result when resolution along the column direction is reduced. On the other hand, at the expense of imaging time or volume coverage, thin-section, submillimeter spatial in-plane resolution can be achieved. Reduction of the bandwidth does increase the signal-to-noise ratio; however, at very low bandwidths, chemical shift and susceptibility artifacts may become an important issue. Other techniques that yield diffusion-weighted images with low susceptibility artifacts are available; for example, multishot navigated echo-planar imaging (20), fast spin-echo (21), magnitude back-projection imaging (22), and single-shot echo-planar imaging with sensitivity encoding (23) have been used in conjunction with diffusion-weighted imaging. However, these techniques are either sensitive to motion and require cardiac gating or suffer from low signal-to-noise ratio.

To visualize the white matter fiber direction with diffusion tensor data, several methods have been proposed. Display of the diffusion ellipsoid, including 3D rendering of diffusion ellipsoids (10), directionally encoded color maps (13, 24), and mapping of the first eigenvectors (12, 16, 25–27), has been suggested previously. To visualize eigenvectors for each pixel, however, 3D volume rendering and shading of the diffusion ellipsoids require very high resolution and fast computer displays. In directionally encoded color maps, it is difficult to follow in-plane connectivity of the same fiber tract group. For optimal visualization, eigenvector directions should be displayed in three dimensions. For example in an axial plane, fibers in the posterior limb of the internal capsule point out of the plane, whereas the anterior limb fibers run parallel to the plane (Fig 4). However, displaying directions in three dimensions with color encoding (13) is not intuitively apparent, because without referring to the definition of the color-encoded direction in a look-up table, the viewer has no clue about the true direction. Our maps of the first eigenvector show fibers running out of the plane as dots. The introduction of dots for eigenvectors pointing out of the plane simulates an ideal cut surface of longitudinal fiber bundles. Therefore, one can easily understand the directional differences not only between in-plane and through-plane but also among different in-plane fiber directions. Moreover, the display of the first eigenvectors presents pictures extremely similar to those shown in anatomy atlas books (14, 15). For good visual impression, the lines need to have a certain length. This may result in lines that exceed the pixel boundaries, and for that reason, it may be less quantitative than a color-encoded map. In recent studies of diffusion tensor imaging, diffusion tracking techniques in humans (28–31) have been introduced. Such techniques are very useful for following white matter fibers from a certain area to another in three dimensions. Connectivity of white matter fibers passing through the entire brain can be visualized with this technique.

Dense and compact white matter pathways, such as the anterior commissure, corpus callosum, superior fronto-occipital fasciculus, cingulum, fornix, mammillothalamic tract, uncinate fasciculus, and superior and inferior longitudinal fasciculus have been identified on conventional and fast spin-echo T2-weighted images by their relative short T2 relaxation time (32, 33). The large bundles of white matter fiber tracts including pyramidal tract (internal capsule to corona radiata) (34), corpus callosum, cingulum (13, 24, 35–37), and optic tract (25) have previously been shown

by other authors. The course of the pyramidal tract within the brain stem has not previously been shown with diffusion tensor imaging. Other small nerve structures, hitherto not observed with diffusion tensor imaging, are the strionigral and pallidonigral fibers, root fibers of the oculomotor nerve, arcuate fibers of the sensory decussation, and superior part of the anterior commissure.

Within the nuclei and deep gray matter, preferred diffusion directions were observed. Diffusion anisotropy in these areas, however, was not as high as in white matter tracts. This anisotropy may be explained by partial volume effects of fibers passing adjacent to the section, but it may also result from smaller radiation fibers connecting to the nucleus (eg, strionigral and pallidonigral fibers). For example, in the coronal image of the midthalamus, we observed well-organized eigenvectors in the area of the thalamic nuclei (ie, an area where partial volume effects of white matter in an adjacent section is unlikely) (Fig 2C).

Diffusion tensor images in this study were obtained at high resolution. Nonetheless, it is not sufficient to resolve all known anatomic structures of the brain. For example, the internucleus fibers could not be distinguished from radiation fibers extending to the larger bundles. The visualization of the tracts varied among participants. However, we attribute this variation not only to individual differences among participants but also to section orientation and position.

Diffusion imaging has been used to diagnose stroke (17, 38, 39) and to investigate brain tumors (40) and multiple sclerosis lesions (41). To better understand the functional consequences of such lesions, detailed knowledge of the fibers surrounding the lesions is needed. In planning of brain tumor surgery, the spatial relation between a lesion and major fiber structures, such as the pyramidal tract, can be very important. Disruption of the normal white matter fibers adjacent to the lesions can be visualized with maps or tracking of the principal diffusion direction. Moreover, there is potential to distinguish preserved white matter fibers within edema from actually disrupted fibers.

Conclusion

We have shown high-resolution white matter fiber anatomy in the human adult brain by using maps of the first diffusion eigenvector. The direction of the first diffusion eigenvector seems to represent the fiber structures shown in anatomy atlases. Unlike directionally encoded color maps, the directional information was displayed with lines drawn on top of conventional images. With line scan diffusion imaging, high-resolution diffusion tensor images with minimal susceptibility artifacts were collected. Particularly near large bone structures (eg, skull base), the low sensitivity to susceptibility variations is important to obtain artifact-free images.

References

1. Ting YL, Bendel P. **Thin-section MR imaging of rat brain at 4.7T.** *J Magn Reson Imaging* 1992;2:393–399
2. Ghosh P, O'Dell M, Narasimhan PT, Fraser SE, Jacobs RE. **Mouse lemur microscopic MRI brain atlas.** *Neuroimage* 1994;1:345–349
3. De Coene B, Hajnal JV, Pennock JM, Bydder GM. **MRI of the brain stem using fluid attenuated inversion recovery pulse sequences.** *Neuroradiology* 1993;35:327–331
4. Wolff SD, Balaban RS. **Magnetization transfer contrast (MTC) and tissue water proton relaxation in vivo.** *Magn Reson Med* 1993; 29:77–83
5. Balaban RS, Ceckler TL. **Magnetization transfer contrast in magnetic resonance imaging.** *Magn Reson Q* 1992;8:116–137
6. Mehta RC, Pike GB, Enzmann DR. **Magnetization transfer MR of the normal adult brain.** *AJNR Am J Neuroradiol* 1995;16:2085–2091
7. Beaulieu C, Allen PS. **Determinants of anisotropic water diffusion in nerves.** *Magn Reson Med* 1994;31:394–400
8. Basser PJ, Mattiello J, LeBihan D. **MR diffusion tensor spectroscopy and imaging.** *Biophys J* 1994;66:259–267
9. Basser PJ, Mattiello J, LeBihan D. **Estimation of the effective self-diffusion tensor from the NMR spin echo.** *J Magn Reson B* 1994;103:247–254
10. Pierpaoli C, Jezzard P, Basser PJ, Barnett A, DiChiro G. **Diffusion tensor MR imaging of the human brain.** *Radiology* 1996;201:637–648
11. Gudbjartsson H, Maier SE, Mulkern RV, Morocz IA, Patz S, Jolesz FA. **Line scan diffusion imaging.** *Magn Reson Med* 1996;36:509–519
12. Peled S, Gudbjartsson H, Westin CF, Kikinis R, Jolesz FA. **Magnetic resonance imaging shows orientation and asymmetry of white matter fiber tracts.** *Brain Res* 1998;780:27–33
13. Pajevic S, Pierpaoli C. **Color schemes to represent the orientation of anisotropic tissues from diffusion tensor data: application to white matter fiber tract mapping in the human brain.** *Magn Reson Med* 1999;42:526–540
14. DeArmond SJ, Fusco MM, Dewey MM. *Structure of the Human Brain: A Photographic Atlas.* 3rd ed. New York: Oxford University Press; 1989
15. Carpenter MB. *Core Text of Neuroanatomy.* 4th ed. Baltimore: William & Wilkins; 1996
16. Huppi PS, Maier SE, Peled S, et al. **Microstructural development of human newborn cerebral white matter assessed in vivo by diffusion tensor magnetic resonance imaging.** *Pediatr Res* 1998;44:584–590
17. Maier SE, Gudbjartsson H, Patz S, et al. **Line scan diffusion imaging: characterization in healthy subjects and stroke patients.** *AJR Am J Roentgenol* 1998;171:85–93
18. Turner R, Le Bihan D, Maier J, Vavrek R, Hedges LK, Pekar J. **Echo-planar imaging of intravoxel incoherent motion.** *Radiology* 1990;177:407–414
19. Davis TL, Wedeen VJ, Weisskoff RM, Rosen BR. **White matter tract visualization by echo-planar MRI.** *ISMRM Proc* 1993:289
20. Bammer R, Stollberger R, Augustin M, et al. **Diffusion-weighted imaging with navigated interleaved echo-planar imaging and a conventional gradient system.** *Radiology* 1999;211:799–806
21. Alsop DC. **Phase insensitive preparation of single-shot RARE: application to diffusion imaging in humans.** *Magn Reson Med* 1997;38:527–533
22. Trouard TP, Theilmann RJ, Altbach MI, Gmitro AF. **High-resolution diffusion imaging with DIFRAD-FSE (diffusion-weighted radial acquisition of data with fast spin-echo) MRI.** *Magn Reson Med* 1999;42:11–8
23. Bammer R, Keeling SL, Augustin M, et al. **Improved diffusion-weighted single-shot echo-planar imaging (EPI) in stroke using sensitivity encoding (SENSE).** *Magn Reson Med* 2001;46:548–554
24. Makris N, Worth AJ, Sorensen AG, et al. **Morphometry of in vivo human white matter association pathways with diffusion-weighted magnetic resonance imaging.** *Ann Neurol* 1997;42:951–962
25. Werring DJ, Clark CA, Parker GJ, Miller DH, Thompson AJ, Barker GJ. **A direct demonstration of both structure and function in the visual system: combining diffusion tensor imaging with functional magnetic resonance imaging.** *Neuroimage* 1999;9:352–361
26. Maier SE, Jolesz FA. **Line scan diffusion imaging with a high performance gradient system.** *ISMRM Proc* 1998:1389
27. Tuch DS, Weisskoff RM, Belliveau JW, Wedeen VJ. **High resolution diffusion imaging of the human brain.** *ISMRM Proc* 1999; 321:30

28. Parker GJ. **Tracing fiber tracts using fast marching.** *ISMRM Proc* 2000;1:85
29. Conturo TE, Lori NF, Cull TS, et al. **Tracking neuronal fiber pathways in the living human brain.** *Proc Natl Acad Sci U S A* 1999;96:10422–10427
30. Poupon C, Clark CA, Frouin V, et al. **Regularization of diffusion-based direction maps for the tracking of brain white matter fascicles.** *Neuroimage* 2000;12:184–195
31. Mori S, Kaufmann WE, Pearlson GD, Crain BJ, Solaiyappan M, van Zijl PC. **Three-dimensional reconstruction of in-vivo human white matter tracts.** *ISMRM Proc* 2000:83
32. Curnes JT, Burger PC, Djang WT, Boyko OB. **MR imaging of compact white matter pathways.** *AJNR Am J Neuroradiol* 1988;9: 1061–1068
33. Cellerini M, Konze A, Caracchini G, Santoni M, Dal Pozzo G. **Magnetic resonance imaging of cerebral associative white matter bundles employing fast-scan techniques.** *Acta Anat (Basel)* 1997; 158:215–221
34. Virta A, Barnett A, Pierpaoli C. **Visualizing and characterizing white matter fiber structure and architecture in the human pyramidal tract using diffusion tensor MRI.** *Magn Reson Imaging* 1999; 17:1121–1133
35. Shimony JS, McKinstry RC, Akbudak E, et al. **Quantitative diffusion-tensor anisotropy brain MR imaging: normative human data and anatomic analysis.** *Radiology* 1999;212:770–784
36. Thompson MR, Venkatesan R, Kuppusamy K, et al. **Increased-contrast, high-spatial-resolution, diffusion-weighted, spin-echo, echo-planar imaging.** *Radiology* 1999;210:253–259
37. Jones DK, Simmons A, Williams SC, Horsfield MA. **Non-invasive assessment of axonal fiber connectivity in the human brain via diffusion tensor MRI.** *Magn Reson Med* 1999;42:37–41
38. Warach S, Chien D, Li W, Ronthal M, Edelman RR. **Fast magnetic resonance diffusion-weighted imaging of acute stroke.** *Neurology* 1992;42:1717–1723
39. Sorensen AG, Wu O, Copen WA, et al. **Human acute cerebral ischemia: detection of changes in water diffusion anisotropy by using MR imaging.** *Radiology* 1999;212:785–792
40. Mamata H, Mamata Y, Jolesz FA, Maier SE. **Line scan diffusion high-resolution tensor images in normal and pathologic brain.** *ISMRM Proc* 2000;2:787
41. Werring DJ, Clark CA, Barker GJ, Thompson AJ, Miller DH. **Diffusion tensor imaging of lesions and normal-appearing white matter in multiple sclerosis.** *Neurology* 1999;52:1626–1632